Journal of Materials Chemistry A

ROYAL SOCIETY OF CHEMISTRY

PAPER

View Article Online
View Journal | View Issue

Cite this: J. Mater. Chem. A, 2022, 10, 22245

Materials design principles of amorphous cathode coatings for lithium-ion battery applications†

Jianli Cheng, [ab] Kara D. Fong [bc] and Kristin A. Persson [*ab]

Received 30th July 2022
Accepted 30th August 2022

DOI: 10.1039/d2ta06051e

rsc.li/materials-a

Cathode surface coatings present one of the most popular and effective solutions to suppress cathode degradation and improve cycling performance of lithium-ion batteries (LIBs). In this work, we carry out an extensive high-throughput computational study to develop materials design principles governing amorphous cathode coating selections for LIBs. Our high-throughput screening includes descriptors to evaluate the thermodynamic stability, electrochemical stability, chemical reactivity with electrolytes and cathodes, and ionic diffusion of the cathode coatings. In the ionic diffusion analysis, we mainly focus on Li-containing compounds. From the 20 selected materials, we highlight the formidable challenge of mitigating oxygen diffusion when selecting an ideal cathode coating, and suggest 7 promising coating candidates: $Li_3B_{11}O_{18}$, $LiZr_2(PO_4)_3$, LiB_3O_5, $LiPO_3$, $LiSb_3O_8$, $LiAlSiO_4$ and $LiTaSiO_5$. Combining the screening results and detailed ionic diffusion analysis of the selected cathode coatings, we summarize the general selection guidelines of amorphous cathode coatings for LIBs.

Introduction

Lithium-ion batteries (LIBs) are ubiquitous in portable electronic devices and have enabled the development of cleaner energy storage and electric vehicles (EVs). For the past decade, LIB-powered EVs have gradually penetrated the automotive market. With an increasing demand of reducing greenhouse gas emissions, the global fleet of EVs will continue to rise for the coming decade.[1] Future improvements in LIBs include high energy density cathode materials to enable longer driving range; however these materials frequently operate at high potential and experience surface degradation with associated performance degradation under extended cycling. The current commercialized cathode materials of LIBs are classified as layered ($LiNi_aCo_bMn_cO_2$, NMC), spinel ($LiMn_2O_4$) and olivine ($LiFePO_4$). Regardless of their crystal structure, these cathode materials all exhibit surface degradation and detrimental surface phase transformations, which compromise the cycle life and thermal stability of LIBs. For example, upon a higher voltage operation (>4.3 V), surface oxygen evolution triggers an irreversible transformation in NMC cathodes from layered phase into a mixture of spinel and rock salt phases that deteriorates capacity retention.[2] Similarly, in $LiMn_2O_4$, surface oxygen loss causes considerable compressive lattice strain, which densifies the cathode surface and blocks the Li-migration pathways.[3] The $LiFePO_4$ cathode exhibits an excellent capacity retention, however, its eventual failure is associated with the surface amorphization and oxygen loss after the prolonged cycling.[4] In addition, side reactions between the electrolyte and cathode lead to transition metals dissolution and surface impedance build-up, which further accelerate the capacity/voltage fade.[5] Therefore, it is of high interest to engineer the cathode surface to achieve high energy density LIBs with a stable, safe, and long-term cycling performance.[5,6]

A common strategy to stabilize the cathode surface is to apply a multifunctional protective layer to mitigate surface degradation and simultaneously maintain facile Li^+ transport.[6] Such cathode coatings typically exhibit an amorphous character, with a thickness between 1 to 10 nm.[7,8] A variety of coating materials have been explored and shown varying degrees of effectiveness in enhancing the cyclability of LIBs, such as metal oxides (*e.g.*, Al_2O_3 (ref. 9)), nonmetal oxides (*e.g.*, B_2O_3 (ref. 10)), polyanionic oxides (*e.g.*, $Li_3B_{11}O_{18}$ (ref. 11)), and fluorides (*e.g.*, AlF_3 (ref. 12)), *etc.* However, several reported cathode coatings have been found to exhibit chemical and/or electrochemical instability and large overpotential during cycling. For example, Al_2O_3 and ZnO effectively mitigate the side reactions of the cathode surface with the electrolyte,[9,13] however, the metal oxide coating layer forms a metal oxyfluoride or a metal fluoride layer by scavenging F^- from HF in the electrolyte.[13,14] Furthermore, because of its inherent low Li^+ ion diffusivity, Al_2O_3 coatings can lead to large overpotentials and reduced capacity, even at a thickness as low as 2 nm.[15,16] On the other hand, Li-containing compounds have been found to exhibit better capacity retention than their non-

[a]Department of Materials Science and Engineering, University of California, Berkeley, CA 94720-1760, USA. E-mail: kapersson@lbl.gov

[b]Energy Storage and Distributed Resources Division, Lawrence Berkeley National Laboratory, Berkeley, CA 94720, USA

[c]Department of Chemical and Biomolecular Engineering, University of California, Berkeley, CA 94720-1760, USA

† Electronic supplementary information (ESI) available. See https://doi.org/10.1039/d2ta06051e

lithiated counterparts, due to their improved ability to transport Li^+.[17] However, a recent study found that an NMC cathode surface still transforms from a layered structure into an oxygen loss-induced rock-salt structure after cycling, even when conformally coated with a $Li_3B_{11}O_{18}$ layer.[11] Similar surface reconstruction phenomenon has been observed in Al_2O_3- and AlF_3-coated cathodes,[12,18] regardless of liquid-electrolyte or solid-electrolyte battery implementations. As different coating materials may enhance one aspect of performance while hindering or falling short of another, ultimately, the question is what are the optimal coating design choices given the battery application, and can we provide a systematic guidance to identify them?

Given the complex reactions between the cathode, coating and electrolyte and the difficulty in deconvoluting experimentally measured solid state ionic diffusion, first-principles modeling provides robust guidelines for new cathode coatings. Aykol *et al.* reported a high-throughput screening of crystalline oxides materials that can stabilize the cathodes in a liquid-electrolyte battery system.[19] However, ionic diffusivity in the coatings was not considered. Liu *et al.* screened Li-containing crystalline fluoride materials and identified 10 promising coating materials along with their calculated Li^+ migration barriers.[20] Xiao *et al.* screened crystalline Li-containing cathode coatings for solid-state batteries and proposed three polyanionic compounds as the most appealing candidates.[21] We note that the ionic diffusion analyses in all previous computational screening work have addressed exclusively the crystalline coating materials, whereas cathode coatings are often amorphous or polycrystalline. In addition, due to their isotropic non-periodic structures, amorphous films tend to be more conformal than polycrystalline films, with reduced grain boundaries, dislocations, or other defect regions.[22] Therefore, amorphous coatings provide a better cathode surface protection against surface oxygen loss and side reactions with electrolytes than polycrystalline coatings. Their unique processability also enables high degrees of interfacial contact with electrodes.[22] Moreover, many amorphous solids, such as Li_3PO_4 and Al_2O_3, have been found to exhibit higher Li^+ conductivity than their crystalline phases.[23,24] However, to our best knowledge, no study has considered O^{2-} diffusion in amorphous films, which is directly related to the oxygen-loss-induced cathode surface densification. In addition, Li^+ and O^{2-} diffusion corresponds to the kinetics of the coatings but has never been applied broadly or systematically enough to derive design rules. In this work, we carry out an extensive high-throughput computational study to develop materials design principles governing amorphous cathode coating selections for LIBs. We evaluate the thermodynamic stability, electrochemical stability, chemical reactivity with electrolytes and cathodes, as well as the Li^+ and O^{2-} diffusion in amorphous cathode coatings. Based on the trends in the screening results and ionic transport, we summarize general guidelines for selecting amorphous cathode coatings.

Computational details

First-principles calculation

All density functional theory (DFT) calculations are performed using the Vienna *Ab initio* Simulation Package (VASP),[25,26] with Projector Augmented Wave (PAW) potentials.[27] The generalized gradient approximation (GGA) as parameterized by the Perdew–Burke–Ernzerhof (PBE)[28] is used for the exchange-correlation functional. For AIMD simulations, we employ Γ-point only Brillouin zone integration at a plane-wave cutoff energy of 400 eV and a time step of 2 fs.

We utilize a "liquid-quench" process to generate the amorphous structures, in which heating, equilibration, and quenching are performed through an AIMD workflow, which can be found as part of the open-source mpmorph package at **https://github.com/materialsproject/mpmorph**. We use the Packmol package[29] to generate all initial amorphous structures. To generate the "liquid" phase of the amorphous structures, we equilibrate the structures at 3000 K using a sequence of 4 ps AIMD simulations in the NVT ensemble until the external pressure and energy are converged. Next, the structures are simulated for an additional 10 ps, from which three independent configurations are selected and quenched to 0 K to obtain the ground-state amorphous structures. To perform ion diffusion analysis, we equilibrate the ground-state structure at $T = 1800$, 2000, 2200, 2400, 2600, and 2800 K, and then simulate an 80 ps diffusion trajectory at each corresponding temperature. The equilibration procedure follows the same steps used to equilibrate the "liquid" amorphous structure. In the end, there are three independent diffusion trajectories at each temperature. Further details about the entire AIMD and DFT workflows can be found in ref. 30.

Self-diffusion coefficients and overpotentials

From the obtained diffusion trajectories, we calculate the self-diffusion coefficients (D) of Li^+ and O^{2-} ions in amorphous structures using the Einstein relation: $D = \frac{1}{6}\mathrm{d}\langle\Delta r^2\rangle/\mathrm{d}t$, where t is the time, r is the ion position and $\langle\Delta r^2\rangle$ is the mean square displacement (MSD). Within the temperature window 1800–2800 K, there are three D values calculated from three independent diffusion trajectories at each temperature. The D values at room temperature are extrapolated from those at high temperatures using the Arrhenius relation of D as a function of T: $D = D_0 \exp(-E_a/k_B T)$, where k_B is the Boltzmann constant, D_0 is the pre-exponential factor and E_a is the activation energy of ion diffusion. In addition, the trajectories at lower temperatures (*e.g.* 1800 K) frequently exhibit fewer ionic hops, which incurs higher statistical uncertainties of fitted D values than those at higher temperatures (*e.g.* 2800 K). Therefore, we consider the uncertainty of the D values at each temperature when linearly fitting $\log D$ *vs.* $1/T$ by assigning the standard deviation of $\log D$ as the uncertainty for each averaged D.

From the calculated room temperature Li^+ diffusivity D_{rt}^{Li}, we estimate the overpotential, ΔV, across a cathode coating layer using a theoretical model which assumes a constant potential gradient, a uniform Li^+ concentration and the Einstein relation to relate Li^+ mobility and diffusion coefficient in the coating.[31,32] The model calculates ΔV as a function of current density, coating thickness, Li^+ concentration, Li^+ diffusivity and temperature, providing a qualitative evaluation on coating's

ability to transport Li^+ ions. The relation between ΔV and D_{rt}^{Li} follows the methodology used in the earlier work,[24,33] namely:

$$\Delta V = \frac{J l_c k_B T}{D_{rt}^{Li} c^{Li} q^2} \quad (1)$$

where l_c is the coating thickness, k_B is the Boltzmann constant, T is the temperature, c^{Li} is the Li^+ concentration in the coating, q is the electron charge, *i.e.*, $q = |e| = 1.602 \times 10^{-19}$ C, and J is the current density through the cathode coating, which results from a flux of Li^+ ions and can be approximated as:[24]

$$J = \frac{\rho V_P C}{S_P t} = \frac{\rho r C}{3t} \quad (2)$$

where ρ is cathode density, V_P is the particle volume, S_P is the particle surface area, r is the particle radius, C is the cathode capacity, and t is the charging/discharging time. Combining eqn (1) and (2), ΔV can be expressed as:

$$\Delta V = \frac{\rho r C}{3t} \frac{l_c k_B T}{D_{rt}^{Li} c^{Li} q^2} \quad (3)$$

In the ESI† we provide the full derivation and assumptions for eqn (1). According to eqn (2), the current density J is normalized by the cathode surface area, while experimentally, J is more commonly normalized by geometric area of the cathode disk. In addition, we assume that the entire spherical cathode particle surface area is available for Li^+ intercalation.

Oxygen flux and transport time

We use the Onsager transport equations to estimate the O^{2-} flux J^O under the driving force of the oxygen chemical potential gradient $\nabla\mu^O$ across the coating layer, which can expressed as:

$$J^O = -L^{OO}\nabla\mu^O \quad (4)$$

where L^{OO} is the Onsager transport coefficient for oxygen transport. It should be noted that in this study we ignore the contributions from cross-correlations between oxygen and other species, such as L^{OLi}, and between distinct oxygen sites, *i.e.* $L^{OO}_{distinct}$, to J^O. We approximate the $\nabla\mu^O$ to be a constant across the thickness of the coating under steady-state conditions. Therefore, eqn (4) can be expressed as:

$$J^O = L^{OO}\frac{\mu_c^O - \mu_e^O}{l_c} \quad (5)$$

where μ_c^O and μ_e^O are the oxygen chemical potential at the cathode and electrolyte sides, respectively. Ignoring the $L^{OO}_{distinct}$ term, L^{OO} can be directly related to the self-diffusion coefficient D^O:[34]

$$L^{OO} \approx L^{OO}_{self} = \frac{D^O c^O}{k_B T} = \frac{D_0^O e^{-\frac{E_a}{k_B T}} c^O}{k_B T} \quad (6)$$

where c^O is the O^{2-} concentration in the coating. The room-temperature L_{rt}^{OO} is extrapolated from L^{OO} values at high temperatures by fitting eqn (6). It should be noted that previous experiments have reported several active oxygen intermediates during oxygen evolution reactions at cathode surface, such as covalent peroxide bonds, oxygen radicals and singlet oxygen ($^1O_2$).[35–37] Because of their high reactivity, we assume these oxygen intermediates will react with the coating materials and become O^{2-}. Therefore, we use O^{2-} diffusion to represent oxygen diffusion in the coatings.

Materials database and descriptors

The entire database used in this study contains 146 323 crystalline compounds, which are queried from the Materials Project (v2021.11.10).[38] The materials properties include DFT calculated total energies, formation energies, energies above convex hull (E_{hull}), band gaps (E_g), *etc.* It should be noted that at zero temperature, the Gibbs free energy of a crystalline polymorph is always lower than that of its amorphous state.[39] However, there is no universal description for the energetics of the amorphous materials, therefore we use the energies of the crystalline phases to approximate the stability of the amorphous phases. Indeed, the distribution of synthesizable crystalline polymorph energies tends to follow the trend of the amorphous energies.[39]

Phase stability. A compound's E_{hull} value is calculated by constructing the convex hull that includes the formation energies of all known crystalline phases in the same chemical space. The compounds that constitute the convex hull, *i.e.* have $E_{hull} = 0$, are deemed stable phases (at low temperature) or ground states for the system studied. The E_{hull} value for metastable phases therefore provides a measure of the driving force for decomposition and a descriptor for the phase stability of each compound.

Electrochemical stability. The calculations of the electrochemical stability window follow the methodology proposed by Aykol *et al.*,[19] which combines DFT formation energies in the Materials Project, experimental thermochemical data for gaseous species and experimental electrochemical data for solvated ions. First, we calculate the standard Gibbs free energy of a reaction (ΔG^0), which is obtained as:

$$\Delta G^0 = G_{products} - G_{reactants} \quad (7)$$

At room temperature, we assume the entropy contributions of solid phases are negligible while the entropy contributions of gaseous species (O_2, F_2, Cl_2, H_2 and N_2) are much higher than that of solid phases. For the gaseous species, their entropy values S at room temperature are taken from the JANAF tables.[40] Thus, ΔG^0 can be approximated as:

$$\Delta G^0 \approx H_{products} - H_{reactants} - T(S_{gaseous\ products} - S_{gaseous\ reactants}) \quad (8)$$

where H represents enthalpy. For solid phases, we assume $P\Delta V$ contributions are negligible and H can be approximated with the DFT calculated internal energy E at 0 K. For gaseous species, we add the anion corrections, which also includes the $P\Delta V$ contribution to their enthalpy.[41] For a reaction involved with solvated ions, we assume a one-step single ion dissolution: $A = A^{n+} + ne^-$ and we add the standard free energy of formation of

a solvated ion, $\Delta G^0_{A^{n+}}$, to ΔG^0 in eqn (8). $\Delta G^0_{A^{n+}}$ can be calculated as:

$$\Delta G^0_{A^{n+}} = -nFE^0_{A^{n+}} \quad (9)$$

where n is the valence state of the ion, F is the Faraday's constant, and $E^0_{A^{n+}}$ is the standard oxidation potential of the A^{n+} ion taken from the IUPAC publication.[42] Next, the free energy of a given reaction can be obtained as:

$$\Delta G = \Delta G^0 + RT \ln \frac{\prod_{\text{products},i} a_i}{\prod_{\text{products},i} a_i} \quad (10)$$

where a_i is the activity of species i. In Aykol's work, they assumed a small activity of $a_{\text{ion}\neq\text{Li}} = 10^{-6}$ for non-Li solvated ions to approximate their dilute concentration in the electrolyte.[19] As this $a_{\text{ion}\neq\text{Li}}$ is arbitrary and its effect on the calculated reaction potential is trivial, *i.e.*, $-0.35/z$, where z is the number of electrons transferred in the reaction, we assumed a_i values of unity for condensed phases and all solvated ions, thus $\Delta G \approx \Delta G^0$. Finally, the reaction potential (*versus* Li metal), V, can be obtained using the Nernst equation:

$$V = -\frac{\Delta G}{zF} \quad (11)$$

Chemical stability. The chemical stability of a cathode coating involves the reactivity of the coating with cathode and electrolyte as described by the reaction energy ΔE_{rxt}.[21,43] For two reactants a and b in contact, the reaction can consume arbitrary amounts of either phase: $xc_a + (1-x)c_b \rightarrow c_{\text{equil}}$, where c_a and c_b are the compositions of a and b normalized by the numbers of atoms, respectively, c_{equil} is the composition of ground-state or phase equilibrium structure determined from the convex hull and x is the mixing parameter between 0 and 1. ΔE_{rxt} is determined with an x that yields the largest reaction driving force: $\Delta E_{\text{rxt}} = \min_{x\in[0,1]}\{E[c_{\text{equil}}] - xE[c_a] - (1-x)E[c_b]\}$.

Results and discussion

Screening process

Fig. 1 illustrates the sequential high-throughput screening procedure for cathode coating materials with descriptors including radioactivity, energy above convex hull (E_{hull}), band gap (E_g), reduction limit (V_{red}), oxidation limit ($-V_{\text{ox}}$), and reaction energy (ΔE_{rxt}) with cathodes and electrolytes.

We exclude compounds containing radioactive elements and categorize the remaining compounds in 8 groups based on their anion chemistry: fluorides, chlorides, oxyfluorides, oxychlorides, metal oxides, nonmetal oxides, polyanionic oxides and others. We use E_{hull} values given in the Materials Project database[38] to screen for the thermodynamically stable compounds and select only the compounds that are on the convex-hull, *i.e.*, $E_{\text{hull}} = 0$. Furthermore, we are interested in electronically insulating coating materials that can block the electron transfer between the cathode and electrolyte and the subsequent electrolyte oxidation at high voltage.[12] Therefore, we exclude all metallic compounds and compounds that exhibit a bandgap, E_g, less than 0.5 eV. However, it should be noted that there is a positive effect of a conductive surface coating on the performance of the cathode, as it provides an electron-conducting media that facilitates the charge transfer at the electrode surface.[44] For example, carbon-coating on $LiFePO_4$ has proven to deliver a higher active material loading and energy density in a full-size battery.[45] The use of E_{hull} and E_g descriptors returns 13 498 compounds for further consideration.

In addition, a coating material that participates in the redox reaction during extensive cycling may cause degradation of the surface film, thus a loss of the surface protection.[15] Therefore, we retain only electrochemically stable compounds that can sustain the desirable voltage window. The electrochemical stability window of a cathode coating represents the voltage range (*versus* Li metal) in which the material is thermodynamically stable upon Li (de)intercalation. It consists of two components: the reduction limit (V_{red}) during discharge and oxidation limit ($-V_{\text{ox}}$) during charge. The reduction (cathodic) limit of a cathode coating with composition $A_aB_bC_c\ldots$ is defined as the voltage limit at which the material lithiates to $A_aB_bC_c\ldots Li_\delta$. The discharge reaction can be expressed as:

$$A_aB_bC_c\ldots + \delta Li^+ + \delta e^- \rightarrow [aA,bB,cC,\ldots,\delta Li]_{\text{min}} \quad (12)$$

where $[a\text{A},b\text{B},c\text{C},\ldots,\delta\text{Li}]$ represents the compositions of the products, which are determined from the stable phases in the relevant phase diagram. δ represents a dilute amount of Li, such that $[a\text{A},b\text{B},c\text{C},\ldots,\delta\text{Li}]$ remains within the first phase-region formed by $A_aB_bC_c\ldots$ and other stable phases towards the Li-node of the phase diagram. In this phase-reigon, $[a\text{A},b\text{B},c\text{C},\ldots,\delta\text{Li}]$ has the lowest Li chemical potential, therefore the highest V_{red}, along the composition path from $A_aB_bC_c\ldots$ towards the Li-node of the phase diagram. For a cathodically stable cathode coating, V_{red} in eqn (12) should be lower than the discharge cutoff voltage of the cathode as shown in Fig. 1. We set the criterion for V_{red} to be 3 V.[19] The oxidation (anodic) limit is defined as the voltage limit at which the material oxidizes and decomposes into one or more phases. The charge reaction can be expressed as:

$$A_aB_bC_c\ldots \rightarrow \delta A^{n+} + n\delta e^- + [(a-\delta)A,bB,cC,\ldots]_{\text{min}} \quad (13)$$

where A^{n+} represents the dissolved ion. For a Li-containing compound, we take Li^+ as the dissolved ion due to its high standard oxidation potential (3.04 V). For a compound that does not contain Li, we determine the dissolved ion by calculating the reaction potentials for all elements in the compound and conservatively selecting the element that leads to the highest reaction potential, thus the highest dissolution tendency. It should be noted that in this study, we assume a one-step single ion dissolution while the actual dissolution process may involve multi-step/multi-ion dissolution. For a non-Li-containing compound with ion dissolution reactions involving other species, we use the oxidation limit of the lithiated, stable compound with the lowest Li chemical potential along the composition path from the compound towards the Li-node of the phase diagram. For example, the dissolution reaction of boron is $B(s) + 3H_2O \rightarrow B(OH)_3(aq) + 3H^+ + 3e^-$ and the

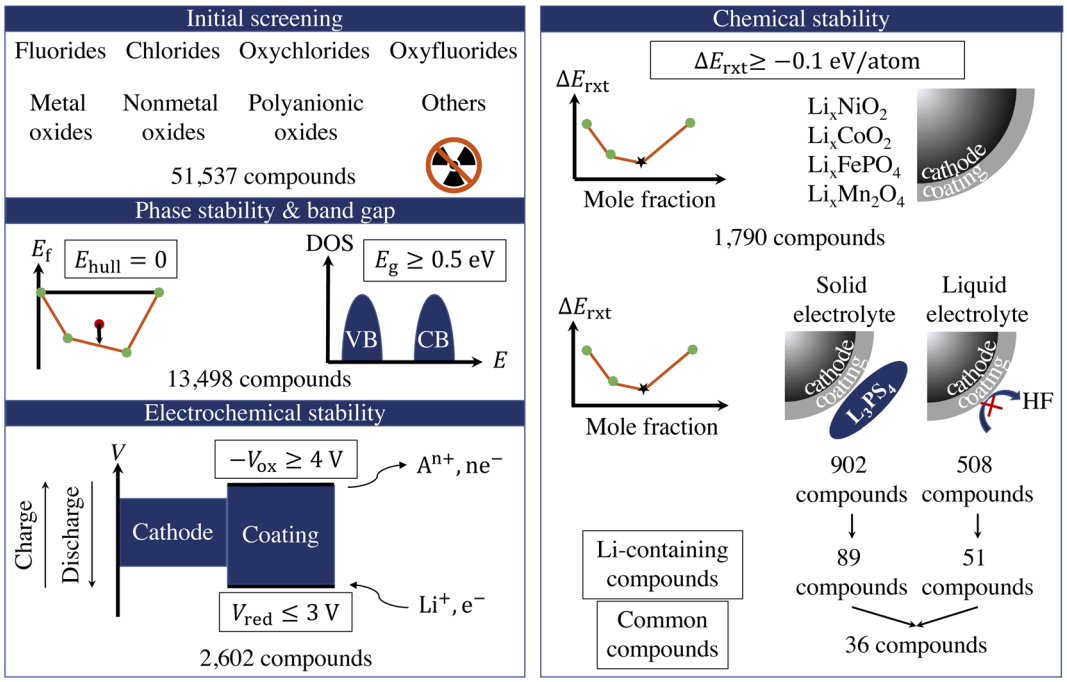

Fig. 1 The flowchart of the high-throughput computational screening of cathode coating materials. Compounds with radioactivity or energy above convex hull (E_{hull}) greater than 0 are excluded. Compounds with band gap (E_g) smaller than 0.5 eV are excluded. Compounds with reduction limit (V_{red}) above 3 V or oxidation limit ($-V_{ox}$) below 4 V are excluded. Compounds with reaction energy (ΔE_{rxt}) with cathode or electrolyte smaller than −0.1 eV per atom are excluded.

oxidation limit of B_2O_3 is estimated using the $-V_{ox}$ value of $Li_3B_{11}O_{18}$. In the ESI,† we illustrate the procedures of calculating [V_{red}, $-V_{ox}$] for $LiAl_5O_8$, Al_2O_3 and B_2O_3 coatings. For a cathode coating to be electrochemically stable during charge, its $|V_{ox}|$ magnitude should be larger than the charge cutoff voltage of the cathode, as shown in Fig. 1. As the oxidation reaction processes are likely to exhibit slow kinetics, an overpotential is expected during the charging cycle. Therefore, we set $|V_{ox}|$ to be 4 V, even though a typical cathode material can be charged up to as high as 4.5 V. The use of electrochemical stability descriptor returns 2602 compounds for further consideration. Fig. 2a illustrates the reduction and oxidation limits of the compounds that are thermodynamically stable. The electrochemical stability of each category is denoted by two violin plots: the left and right represent oxidation and reduction limits, respectively. We find that in general, fluorides, such as AlF_3 and $LiAlF_4$, have the largest electrochemical stability window with high oxidation limits and low reduction limits. On the other hand, metal oxides, such as BaO and Bi_2O_3, exhibit low oxidation limit, and nonmetal oxides, such as P_2O_5 and SeO_2, have high reduction limit. The bar graph in Fig. 2a summarizes the numbers of compounds for each category of materials that pass the electrochemical stability screening. After this screening tier, polyanionic oxides have the largest number of candidates, followed by fluorides and chlorides. There are only 12 metal oxides and 1 nonmetal oxide, B_2O_3, left for further screening.

The fourth attribute we consider is the chemical stability of the cathode coatings. It has been shown that a coating material can react with cathodes and electrolytes to form new phases at cathode/coating and coating/electrolyte interfaces, respectively.[7,16] Therefore, we screen for cathode coatings that are inert to chemical reactions with both cathodes and electrolytes. The reaction energy ΔE_{rxt} is calculated using DFT-computed energies of the reactants and products, and a more negative ΔE_{rxt} indicates a more reactive chemical reaction. We set the criterion for chemically stable cathode coatings as: $\Delta E_{rxt} \geq -0.1$ eV per atom.[21] We calculate ΔE_{rxt} between cathodes and coating materials using the commonly used cathodes, layered $LiNiO_2$ and $LiCoO_2$, spinel $LiMn_2O_4$, and olivine $LiFeOP_4$. Both lithiated and half-lithiated cathodes are considered corresponding to the discharge and charge cycles, respectively. We select the most negative ΔE_{rxt}, *i.e.*, the most favorable chemical reaction, as the $\Delta E_{rxt}^{cathodes}$ for each compound, and we plot $\Delta E_{rxt}^{cathodes}$ for each category that pass the electrochemical stability descriptor in Fig. 2b. In Fig. S2,† we also plot ΔE_{rxt} of each selected cathode material. We find that compared with other cathodes, $LiNiO_2$ tends to exhibit a more negative ΔE_{rxt}, therefore reacts more favorably with the coating materials. In addition, oxides coatings are less prone to react with cathodes than fluorides and chlorides. Specifically, all the electrochemically stable metal oxides exhibit low reactivity with common cathodes and pass the chemical stability descriptor. This round of screening returns 1790 compounds for further consideration with polyanionic oxides having the largest number of candidates (714).

Similarly, we calculate ΔE_{rxt} between coating materials and representative electrolyte components. In this study, we consider the commonly used Li_3PS_4 solid electrolyte and $LiPF_6$-

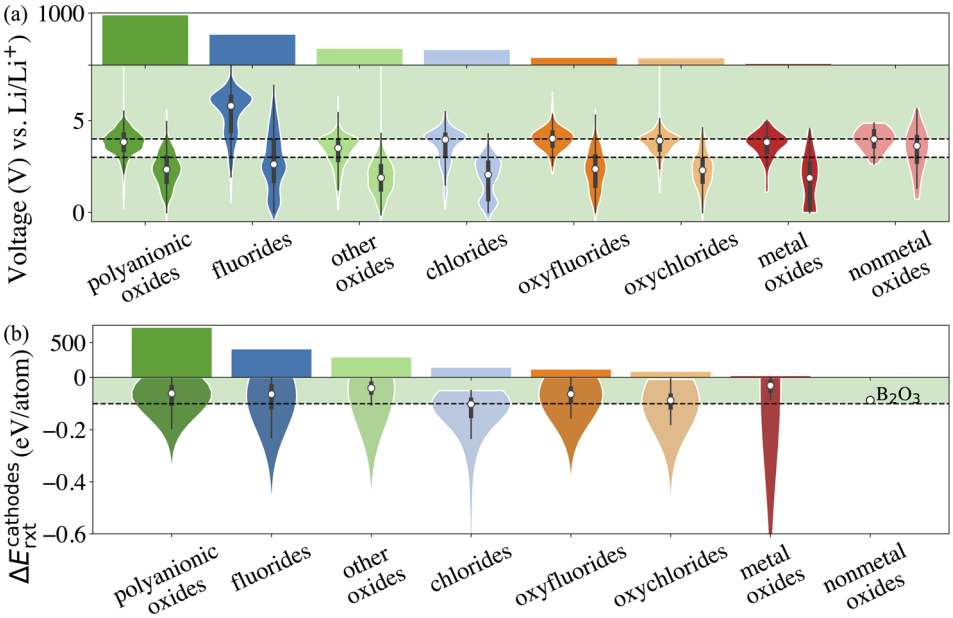

Fig. 2 (a) Distribution of the reduction and oxidation limits for each category that pass thermodynamic stability descriptor. (b) Distribution of the reaction energy ΔE_{rxt} with $LiNiO_2$, $LiCoO_2$, $LiMn_2O_4$ and $LiFeOP_4$ cathodes for each category that pass electrochemical stability descriptor. Both lithiated and half-lithiated cathodes are evaluated and the most negative ΔE_{rxt} is selected as ΔE_{rxt} with cathodes. The horizontal dash lines represent the limits of the descriptors. The histograms in (a) and (b) illustrate the numbers of compounds for each category that pass the descriptors.

based non-aqueous liquid electrolytes, respectively, and categorize the coating materials based on their reactivity. In the case of $LiPF_6$-based electrolytes, we calculate ΔE_{rxt} between coating materials and HF, which is known to react strongly with both cathodes and coating materials. Fig. 3 illustrates the distribution of ΔE_{rxt} with Li_3PS_4 and HF for the compounds that are chemically stable with the cathodes. We find that most fluorides and chlorides have lower chemical reactivity with both Li_3PS_4 and HF than oxides compounds, thus are chemically compatible with both the cathodes and electrolytes. On the other hand, most oxides compounds are not chemically inert in $LiPF_6$-based liquid electrolytes due to a high reactivity with HF. It should be noted that these chemical reactions may only happen at the coating/electrolyte interface and render a partially fluorinated oxides coating layer, which could be beneficial for the cycling performance.[46] Therefore, even though we categorize the coatings based their chemical compatibility with liquid and solid electrolyte, the materials may be effective in both conditions. It should be noted that in $LiPF_6$-based liquid electrolyte systems, besides fluorination of the coating layer from an HF attack, other organic species and Li_2CO_3 can also be found on the surface of the coated cathodes. We only consider the HF attack to broadly capture the chemical compatibility between coatings and $LiPF_6$-based liquid electrolytes in a high-throughput fashion. This round of screening returns 902 and 508 coating candidates that are chemically compatible with Li_3PS_4 and $LiPF_6$ based electrolytes, respectively.

In this study, we are mainly interested in the Li-containing compounds, as lithiated compounds tend to exhibit a higher ionic conductivity.[30] Adding the Li-containing criterion, the entire screening procedure returns 89 and 51 Li-containing compounds that pass the proposed criteria for stability with respect to Li_3PS_4 solid state electrolyte and HF, respectively, with 36 compounds that are chemically compatible with both Li_3PS_4 and HF. In Fig. S2,† we summarize the numbers of Li-containing compounds for each category that pass the phase stability, electrochemical stability, and chemical stability descriptors. We find that oxides coatings, especially polyanionic oxides, account for the largest number of coatings for Li_3PS_4-based LIB, followed by fluorides and chlorides. On the other hand, the majority of coatings for $LiPF_6$-based LIB are fluorides and chlorides. The common coatings only consist of the fluorides and chlorides. In Table S3,† we list the calculated voltage windows, reduction and oxidation reactions, and reaction energies for the 104 Li-containing compounds that pass the screening criteria. In ESI,† we list the calculated material attributes of coating candidates.

Ion diffusion analysis

Our computational screening procedure has narrowed down the coatings of interest to 104 Li-containing compounds. Besides providing facile Li^+ diffusion pathways, an optimal cathode coating should block O^{2-} diffusion such that the oxygen-loss-induced cathode surface reconstruction can be mitigated. Therefore, to evaluate Li^+ and O^{2-} transport in the screened amorphous coatings, we calculate ionic diffusivity, flux, and transport time through the coating materials using *ab initio* molecular dynamics (AIMD) simulations and Onsager transport models, as described in Computational details. Due to the high computational cost of investigating the ionic

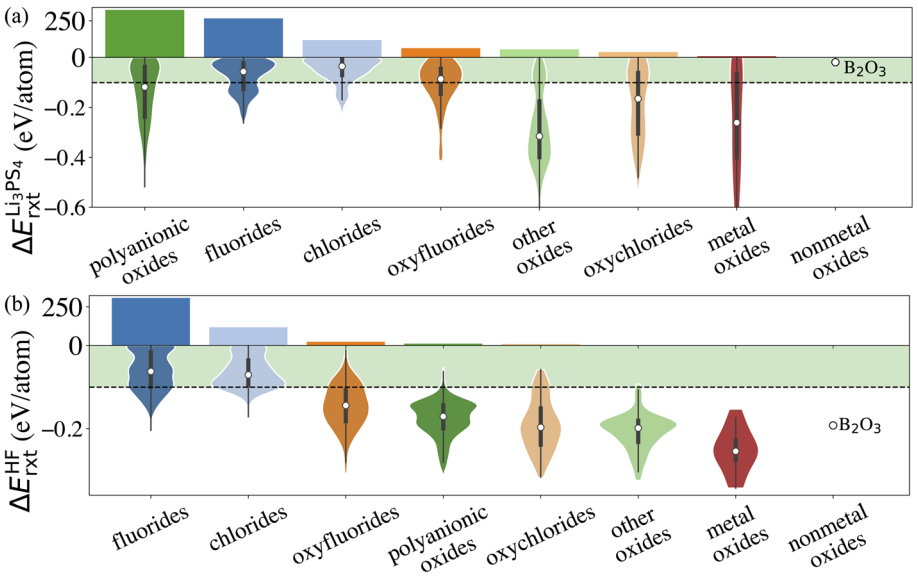

Fig. 3 Distribution of the reaction energy ΔE_{rxt} with Li_3PS_4 (a) and HF (b) for each category that pass chemical stability with the cathodes descriptor. The horizontal dash lines represent the limits of the descriptors. The histograms in (a) and (b) illustrate the numbers of compounds for each category that pass the descriptors.

diffusivity of all promising coating candidates, we select 9 representative compounds, consisting of polyanionc oxides $Li_3B_{11}O_{18}$, $LiZr_2(PO_4)_3$, Li_3PO_4, $Li_2B_3PO_8$ and LiB_3O_5, fluorides Li_3AlF_6, $LiCaAlF_6$, $LiYF_4$ and chloride Li_2ZnCl_4, and analyze their ion diffusion. Fig. 4 illustrates the distribution of D_{rt}^{Li} and D_{rt}^{O} in the selected compounds, along with 7 Li-containing compounds that are filtered out by electrochemical or chemical stability criterion: $LiNbO_3$, Li_2HfO_3, $LiAlO_2$, $LiTaSiO_5$, $LiPO_3$, $LiAlSiO_4$, and $LiSb_3O_8$, and 4 binary oxides: Li_2O, ZnO, Al_2O_3, Sb_2O_5. Our calculations show that in general, Li^+ and O^{2-} diffusion is correlated, *i.e.*, a compound with a higher D_{rt}^{Li} also has a higher D_{rt}^{O}. For example, the D_{rt}^{Li} and D_{rt}^{O} in Li_3PO_4 are 10^{-9} and 10^{-10} cm^2 s^{-1}, respectively, both of which are higher than those in $LiAlSiO_4$ ($D_{rt}^{Li} = 10^{-14}$ cm^2 s^{-1}, $D_{rt}^{O} = 10^{-23}$ cm^2 s^{-1}). The correlation between Li^+ and O^{2-} diffusion can be explained by ionic conduction mechanism in amorphous structures. Our previous study[30] showed that Li^+ and O^{2-} diffusion consists of discrete vibrational and translational motions. During vibrational motions, Li^+ is bonded to more O^{2-} ions than during translational motions, and its translation to another vibration site is activated by the Li–O bond breaking/formation process, which effectively explains the correlated transport between Li^+ and O^{2-}. In addition, we find that for compounds consisting of the same species, a compound with a higher Li^+ concentration also has a higher Li^+ and O^{2-} diffusion. For example, comparing $Li_3B_{11}O_{18}$ and LiB_3O_5, we find that LiB_3O_5, which has a higher Li^+ concentration, exhibits a higher D_{rt}^{Li} and D_{rt}^{O}. Similar behavior is found in $LiPO_3$ and Li_3PO_4, relating to their D_{rt}^{Li} and D_{rt}^{O}. Our results are consistent with Xu *et al.*'s work in which they found that a higher Li^+ solubility will enhance the Li^+ transport across the coating.[24] In our work, we further demonstrate that, unfortunately, a higher Li^+ concentration also correlates with increased, detrimental O^{2-} transport.

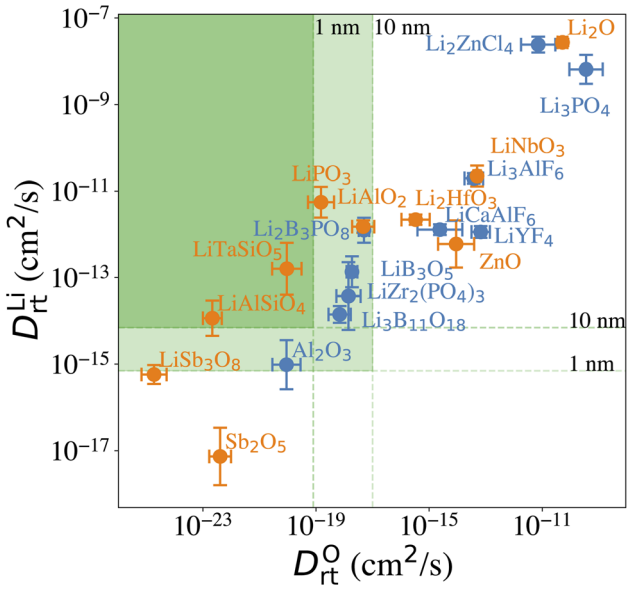

Fig. 4 Calculated room-temperature self-diffusion coefficients of Li^+ (D_{rt}^{Li}) and O^{2-} (D_{rt}^{O}) in the selected compounds. The dash lines represent the approximated D_{rt}^{Li} and D_{rt}^{O} limits based on a coating thickness between 1 to 10 nm.

From the calculated D_{rt}^{Li} and D_{rt}^{O}, we evaluate the coating suitability of the selected compounds in terms of their ability to facilitate Li^+ transport while blocking O^{2-} transport. Low Li^+ diffusivity within the cathode coating layer can increase resistance and capacity loss at higher C-rates due to the resulting large overpotential at higher currents.[47] Thus, for the selected coating compounds, we estimate the overpotential, ΔV, at the cathode surface. We set the criterion for overpotential imposed by the coating as $\Delta V \leq 0.1$ V, above which the Li^+ transport

across the coating will be significantly compromised. In this study, we choose $LiNiO_2$ as the relevant cathode material, with density $\rho = 4.78$ g cm^{-3} and a theoretical capacity $C = 274$ mA h g^{-1}. Eqn (3) shows that a smaller ΔV can be realized by reducing the cathode particle size and coating thickness, and selecting a coating with high Li^+ diffusivity D_{rt}^{Li} and concentration c^{Li}. By assuming a radius $r = 1$ μm $LiNiO_2$ primary particle and a 1C rate current density through the coating, the current density J is estimated to be 0.044 mA cm^{-2}. Finally, using D_{rt}^{Li} and the Li^+ concentration of the compounds, we calculate the ΔV values across a 1 and 10 nm conformal coating, respectively. Fig. 5a shows that for 1 nm surface coatings, all the selected compounds, except Sb_2O_5 (23 V) and $LiSb_3O_8$ (0.18 V), result in overpotentials below 0.1 V, which indicates a sufficient Li^+ transport in these compounds. The overpotential of the Al_2O_3 coating is found to be 0.07 V. When the coating thickness is increased to 10 nm, the overpotentials of Sb_2O_5, $LiSb_3O_8$ and Al_2O_3 coatings increase to 230 V, 1.8 V and 0.7 V, respectively, while the overpotentials of other compounds are still below 0.1 V. Using an $r = 1$ μm $LiNiO_2$ primary particle in a 1C rate current density, we estimate the minimum Li^+ diffusivity D_{rt}^{Li} to meet the overpotential criterion of $\Delta V \leq 0.1$ V. By assuming a Li^+ concentration $c^{Li} = 10^{22}$ cm^{-3}, we find that $D_{rt}^{Li} = 7 \times 10^{-16}$ cm^2 s^{-1} and 7×10^{-15} cm^2 s^{-1} for a 1 and 10 nm cathode coating, respectively, which are represented by the horizontal dashed lines in Fig. 4.

To evaluate the effectiveness of these coatings in blocking O^{2-} transport, we estimate the O^{2-} flux J^O and the time t required for O^{2-} to diffuse through the coating. We assume the oxygen-loss-induced surface rocksalt layer mainly consists of NiO, which is densified from the layered NiO_2. As $NiO_2 \rightarrow NiO + 1/2O_2$, we estimate t for surface NiO_2 layer to lose half of its oxygen and transform into an NiO layer. Let c_{max}^O denote the O^{2-} concentration in NiO_2 and V_s represent the shell volume of the surface NiO layer. $V_s = \frac{4}{3}\pi[r^3 - (r - l_s)^3]$, where l_s is the thickness of the surface NiO layer. Thus, the upper bound value of the number of O^{2-} ions removed from the cathode surface is $N = 0.5V_s c_{max}^O$ and the O^{2-} diffusion time t can be expressed as:

$$t = \frac{N}{S_P J^O} = \frac{0.5 V_s c_{max}^O}{S_P J^O} \quad (14)$$

where $S_P = 4\pi r^2$ is the cathode particle surface area. Combining eqn (14) and (15), t can be expressed as:

$$t = \frac{0.5 V_s}{S_P} \frac{c_{max}^O l_c}{L^{OO}(\mu_c^O - \mu_e^O)} = \frac{r^3 - (r - l_s)^3}{6(r + l_c)^2} \frac{c_{max}^O l_c}{L^{OO}(\mu_c^O - \mu_e^O)}. \quad (15)$$

μ_c^O can be estimated from the cathode densification reaction consistent with the phase diagram. At a high charge state, layered NiO_2 would densify to rocksalt NiO and spinel Ni_3O_4 with oxygen being released at $\mu_c^O = -4.95$ eV, which is equal to the DFT-calculated total energy of an O_2 atom. μ_e^O can be estimated from two different conditions: (1) using the condition where the electrolyte reacts with O^{2-} and forms a new compound (Li_3PS_4 reacts with O^{2-} and forms Li_3PO_4 at $\mu_e^O = -8.39$ eV) and (2) using the condition where O^{2-} loses electrons to the carbon network and forms O_2 (at room temperature and $PO^2 = 0.21$ atm, $\mu_e^O = -5.24$ eV). Thus, we estimate $-8.39 \leq \mu_e^O \leq -5.24$ eV. Eqn (15) indicates that for a given cathode coating and a given size of $LiNiO_2$ primary particle, a longer O^{2-} diffusion time t can be realized by a smaller oxygen chemical potential gradient, *i.e.*, higher l_c and μ_e^O. By assuming an $r = 1$ μm $LiNiO_2$ primary particle and an $l_s = 2$ nm surface NiO layer, we estimate the time t for O^{2-} ions to diffuse through the selected coatings (see Fig. 5b). We consider a range of conditions by varying l_c and μ_e^O, with $l_c = 10$ nm, $\mu_e^O = -5.24$ eV

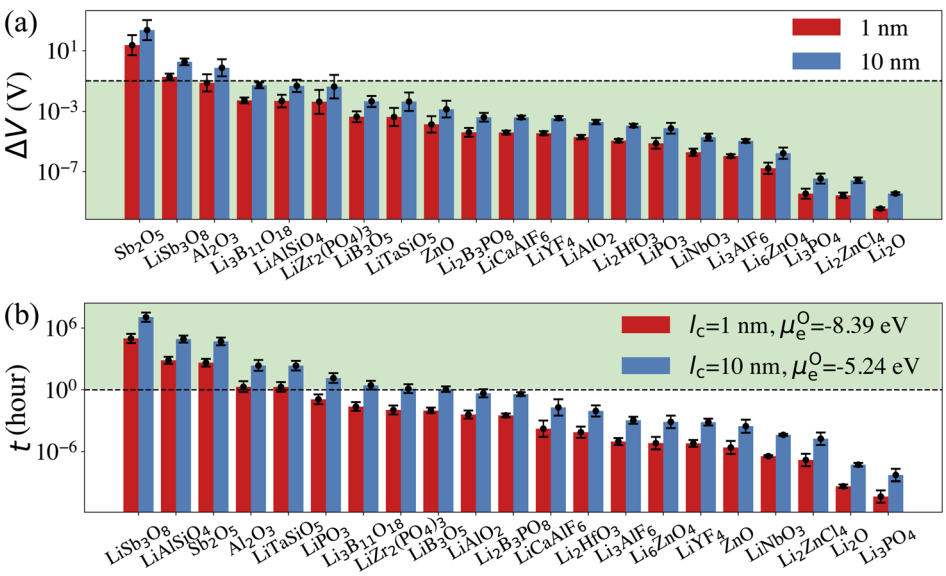

Fig. 5 (a) Calculated overpotentials (ΔV) for a current density of 0.044 mA cm^{-2} across room temperature cathode coatings of $l_c = 1$ and 10 nm. The dashed line represents $\Delta V = 0.1$ V. (b) Calculated O^{2-} diffusion time t in the selected compounds assuming an $r = 1$ μm primary particle and an $l_s = 2$ nm surface rocksalt phase. The dashed line represents $t = 1$ h.

corresponding to the slowest O^{2-} diffusion and $l_c = 1$ nm, $\mu_e^O = -8.39$ eV corresponding to the fastest O^{2-} diffusion. Fig. 5b shows the calculated O^{2-} diffusion time t in the selected compounds. We select the compounds with an estimated O^{2-} diffusion time longer than 1 h such that not all O^{2-} ions that are evolved from surface NiO_2 layer have diffused through the coating under 1C rate. We find that $LiSb_3O_8$, $LiAlSiO_4$, Sb_2O_5, Al_2O_3, $LiTaSiO_5$, $LiPO_3$, $Li_3B_{11}O_{18}$, $LiZr_2(PO_4)_3$ and LiB_3O_5 exhibit an estimated O^{2-} diffusion time longer than 1 h. Next, we estimate the upper limit of O^{2-} diffusivity to have $t \geq 1$ h. As mentioned earlier, we approximate $L_{rt}^{OO} \approx L_{rt,self}^{OO}$. Using eqn (6), we can directly calculate L_{rt}^{OO} from self-diffusion coefficient D_{rt}^O:

$$L_{rt}^{OO} = \frac{D_{rt}^O c^O}{k_B T} = \frac{r^3 - (r - l_s)^3}{6(r + l_c)^2} \frac{c_{max}^O l_c}{t(\mu_c^O - \mu_e^O)} \quad (16)$$

Next, we use the same cathode particle configuration and assume an O^{2-} concentration $c^O = 10^{22}$ cm^{-3} in a coating layer. We find that $D_{rt}^O = 8 \times 10^{-20}$ cm^2 s^{-1} for $l_c = 1$ nm, $\mu_e^O = -8.39$ eV and $D_{rt}^O = 1 \times 10^{-17}$ cm^2 s^{-1} for $l_c = 10$ nm, $\mu_e^O = -5.24$ eV, which are represented by the vertical dashed lines in Fig. 4. Therefore, the green region in Fig. 4 represents the favorable Li^+ and O^{2-} diffusivity window, and a compound falling on the top left area is more desirable in terms of facilitating Li^+ transport while blocking O^{2-} transport. It should be noted that the effect of different cathode materials on ΔV and t is marginal (see Fig. S4†). Therefore, the calculated ΔV, t, and Li^+ and O^{2-} diffusivity window are applicable for other cathodes, such as Ni-based NMC and $LiCoO_2$.

Five observations can be made from the high-throughput screening results and the estimated overpotential ΔV and O^{2-} diffusion time t:

(1) Among the nine Li-containing compounds that pass the computational screening, only $Li_3B_{11}O_{18}$, $LiZr_2(PO_4)_3$ and LiB_3O_5 have been found to exhibit both $\Delta V \leq 0.1$ V and $t \geq 1$ h. However, the thickness of the considered coatings should be large enough (*e.g.* 10 nm) to improve their oxygen-retaining ability. Experimentally, Zhang *et al.* demonstrated that an amorphous $Li_3B_{11}O_{18}$ coating layer with a few nanometers thickness exhibits excellent chemical/electrochemical stability and can significantly improve the capacity retention of NMC cathodes.[11] However, the surface structure of NMC particles still evolved from a layered phase to a rocksalt phase after cycling. Our recent calculations showed facile O^{2-} transport in the amorphous $Li_3B_{11}O_{18}$ material, which leads to an oxygen-loss induced surface phase transition. In this work, we predict that a thicker $Li_3B_{11}O_{18}$ coating layer (*e.g.* 10 nm) is beneficial to mitigate the oxygen-loss induced surface densification and further improve the cycling performance of NMC cathodes. In addition, Wang *et al.* reported that amorphous $LiZr_2(PO_4)_3$ coated $LiCoO_2$ exhibits better capacity retention and rate performance than bare $LiCoO_2$.[48] The enhanced cycling performance was attributed to an enhanced Li-ion diffusion and a significantly mitigated chemical reactions between $LiCoO_2$ and sulfide-based solid electrolytes by the protective $LiZr_2(PO_4)_3$ coating layer, which agrees well with our ion diffusion and chemical stability analysis. However, based on our O^{2-} diffusion in amorphous $LiZr_2(PO_4)_3$ analysis, we expect that the 2 nm $LiZr_2(PO_4)_3$ coating used in their study is not thick enough to mitigate oxygen loss from $LiCoO_2$ surface and it's likely that the $LiCoO_2$ cathodes still suffer from oxygen-loss induced surface reconstruction at prolonged cycling and high charge.[49] Therefore, we predict that a thicker $LiZr_2(PO_4)_3$ coating (*e.g.* 10 nm) could further improve the cycling performance of $LiCoO_2$.

(2) Among the nine Li-containing compounds that do not pass the computational screening, $LiPO_3$, $LiSb_3O_8$, $LiAlSiO_4$ and $LiTaSiO_5$ can also be considered as promising cathode coatings mainly because of their exceptional oxygen retaining ability. $LiPO_3$ exhibits a high oxidation limit (4.9 V) and a reaction energy $\Delta E_{rxt} = -0.11$ eV per atom with $LiNiO_2$ to form $LiNiPO_4$ and Li_3PO_4, therefore is screened out by our chemical stability criterion: $\Delta E_{rxt} \geq -0.1$ eV per atom. However, both $LiNiPO_4$ and Li_3PO_4 coatings have been reported to enhance the rate capability and cycle performance of cathode materials[50,51] and the chemical reaction may only happen at the interface of $LiPO_3$ and $LiNiO_2$ considering the sluggishness of solid state reactions. Experimentally, Chong *et al.*[8] coated $LiNi_{0.5}Mn_{1.5}O_4$ (LNM) particles with a 1 nm thickness of amorphous $LiPO_3$ and found that the $LiPO_3$ coating can significantly reduce the cell impedance and facilitate Li^+ ion transport, which is in good agreement with our calculations. $LiSb_3O_8$ also exhibits a high oxidation limit (5.0 V), but its predicted reduction limit (3.2 V) is higher than our reduction limit criterion: $V_{red} \leq 3$ *V*. However, its lithiated compound $LiSbO_3$ is expected to exhibit a higher Li^+ diffusion, which may offset its relatively high overpotential. In addition, $LiSb_3O_8$ reacts favorably with both HF and LiS_3PS_4, *i.e.* $\Delta E_{rxt} \leq 0.1$ eV per atom. We note that these chemical reactions may only happen at the coating/electrolyte interface and the reaction products could form a passivation layer to prevent further reactions. $LiAlSiO_4$ exhibits excellent oxygen retention, but its oxidation limit ($|V_{ox}| = 3.9$ V) is lower than our oxidation limit criterion: $|V_{ox}| \geq 4$ V. However, $LiAlSiO_4$ decomposition involves the O_2 evolution reaction, which is likely to have sluggish kinetics.[52,53] Therefore, the overpotential of the $LiAlSiO_4$ decomposition reaction may increase its oxidation limit, *i.e.*, $|V_{ox}| \geq 4$ V. Experimentally, Deng *et al.*[54] cycled an amorphous $LiAlSiO_4$-coated LNM cathode with an electrochemical window from 3.5 to 4.9 V for 150 cycles and found improved capacity retention, lower Mn-dissolution and faster Li^+ transport in $LiAlSiO_4$-coated LNM, compared to uncoated LNM. Our calculated Li^+ diffusivity in $LiAlSiO_4$, 1.16×10^{-14} cm^2 s^{-1}, is also in good agreement with their reported value, 7.96×10^{-15} cm^2 s^{-1}. Therefore, despite its limitations, we include $LiAlSiO_4$ in the list of promising cathode coatings. Similarly, $LiTaSiO_5$ is another potentially effective cathode coating, despite its low oxidation limit ($|V_{ox}| = 3.9$ V).

(3) Fluoride and chloride materials exhibit exceptional electrochemical and chemical stability as well as low overpotentials due to their fast Li^+ transport. However, our calculations also show that the fluoride and chloride coatings are O^{2-} transparent, which means that halide-coated cathode surfaces will be

prone to oxygen loss and are likely to transform over time into a densified rocksalt phase.

(4) Although non-Li containing, Al_2O_3 can be considered as a promising cathode coating. We estimate that the diffusion time of oxygen in an Al_2O_3 coating varies between 2 to 227 h, depending on l_c and $\nabla\mu^O$ (see Fig. 4). Thus, we predict that an NMC cathode coated with a thin Al_2O_3 coating layer, such as 1 nm, is still prone to surface oxygen loss, especially when cycled at low C-rate. This result could explain why a 3 nm Al_2O_3 surface coating is not sufficient to stabilize NMC cathode surface when cycled at C/7.[18] On the other hand, a thicker Al_2O_3 coating layer can effectively mitigate O^{2-} transport, which results in a better cathode surface protection; David *et al.* showed that an Al_2O_3 ALD coating can effectively prevent surface reconstruction of NMC cathodes even after 760 cycles,[55] which indicates that a thick and conformal Al_2O_3 coating was applied on the NMC cathodes in their study.

(5) An optimal amorphous cathode coating should not only exhibit sufficient thermodynamic stability, electrochemical stability and chemical stability, but also a low O^{2-} diffusivity and a high Li^+ diffusivity to achieve oxygen-retaining and surface-protective functions while avoiding significant losses in rate capability. However, the correlation between Li^+ and O^{2-} diffusion in amorphous coatings highlights the inherent contradiction in identifying cathode coating materials with optimal Li^+ transport as well as O^{2-} blocking ability. In general, Li^+ diffusion in Li-containing compounds is fast enough to avoid a large overpotential. As a higher Li^+ diffusion may compromise a coating's ability to block O^{2-} diffusion, for compounds with same chemistry, a compound with a lower Li^+ concentration is thus preferred. For example, the Li^+ concentrations in $LiPO_3$ and Li_3PO_4 are 20% and 37.5%, respectively. Fig. 4 shows that both $LiPO_3$ and Li_3PO_4 exhibit a facile Li^+ diffusion, but $LiPO_3$ exhibits an improved oxygen retention as compared to Li_3PO_4. In addition, the oxidation limit of $LiPO_3$ (4.9 V) is higher than that of Li_3PO_4 (4.0 V).

Conclusions

In summary, we have carried out an extensive high-throughput computational study to develop materials design principles governing amorphous cathode coating selections for Li-ion battery applications. Our high-throughput screening includes descriptors to evaluate the thermodynamic stability, electrochemical stability, chemical reactivity with electrolytes and cathodes, and ionic diffusion in the cathode coatings. We consider reactivity with the commonly used Li_3PS_4 solid state electrolyte and with HF as a particularly detrimental representative of liquid electrolyte degradation. We find that polyanionic oxides account for the largest number of cathode coatings for Li_3PS_4-based LIB, followed by fluorides and chlorides. On the other hand, the majority of cathode coatings that are inert to chemical reactions with HF are fluorides and chlorides. Combing the screening results and ionic diffusion analysis of 20 selected compounds, we summarize the promising cathode coatings and general materials design principles:

(1) Li^+ and O^{2-} diffusion are highly correlated, therefore, a higher Li^+ transport promotes higher O^{2-} transport. In Li-containing compounds, the Li^+ diffusion rate is generally fast enough to avoid a large overpotential. When selecting a cathode coating with same chemistry, a compound with a lower Li concentration is preferred, as it exhibits an improved oxygen retention as well as a higher oxidation limit.

(2) Mitigating O^{2-} diffusion is a formidable challenge when selecting an ideal cathode coating as most thin conformal coatings will transport oxygen under prolonged cycling and high voltage. Our results show that in addition to the four experimentally confirmed cathode coatings: $Li_3B_{11}O_{18}$, $LiZr_2(PO_4)_3$, $LiPO_3$ and $LiAlSiO_4$, we also identify three new promising cathode coatings: LiB_3O_5, $LiSb_3O_8$ and $LiTaSiO_5$.

(3) Based on our ionic diffusion analysis, we find that BO_x^{y-}, SiO_x^{y-}, PO_x^{y-} and SbO_x^{y-} anion groups tend to exhibit an improved oxygen retention. Therefore, we expect that compounds such as $LiBa(B_3O_5)_3$, $LiAl(Si_2O_5)_2$, $LiTi_2(PO_4)_3$, $LiScP_2O_7$, $LiK(PO_3)_2$, and $LiCs(PO_3)_2$ could also be potentially effective cathode coatings. On the other hand, F^- and Cl^- anion groups tend to exhibit faster Li^+ and O^{2-} diffusion as compared to the oxides. Thus, they are not ideal for high-voltage cathode coatings where the driving force for oxygen loss is high. However, their inherent fast Li^+ diffusivity may render them promising candidates as the solid-state electrolytes or lithium metal coatings.

(4) A non-Li-containing compound generally exhibits slower Li^+ diffusion but better oxygen retention ability as compared to its lithiated counterpart. We mainly consider Li-containing compounds in this study, however, we expect that effective cathode coatings can also be found in non-lithiated compounds, such as Al_2O_3. Based on our identified anion groups above, we expect that compounds, such as $ScBO_3$, $HfSiO_4$, ZrP_2O_7 and $AlPO_4$, could be potentially effective cathode coatings. A follow-up study on non-Li-containing coatings will be presented in a later report.

Conflicts of interest

There are no conflicts to declare.

Acknowledgements

The authors thank Dr. Gerbrand Ceder and Dr. Muratahan Aykol for useful discussions. This work was intellectually led by the Battery Materials Research (BMR) program under the Assistant Secretary for Energy Efficiency and Renewable Energy, Office of Vehicle Technologies of the U.S. Department of Energy, Contract DEAC02-05CH11231. This research used resources of the National Energy Research Scientific Computing Center (NERSC).

References

1 W. Li, E. M. Erickson and A. Manthiram, *Nat. Energy*, 2020, **5**, 26–34.

2 S.-K. Jung, H. Gwon, J. Hong, K.-Y. Park, D.-H. Seo, H. Kim, J. Hyun, W. Yang and K. Kang, *Adv. Energy Mater.*, 2014, **4**, 1300787.
3 X. Gao, Y. H. Ikuhara, C. A. J. Fisher, R. Huang, A. Kuwabara, H. Moriwake, K. Kohama and Y. Ikuhara, *J. Mater. Chem. A*, 2019, **7**, 8845–8854.
4 M. Gu, W. Shi, J. Zheng, P. Yan, J.-g. Zhang and C. Wang, *Appl. Phys. Lett.*, 2015, **106**, 203902.
5 D. H. Jang and S. M. Oh, *J. Electrochem. Soc.*, 1997, **144**, 3342–3348.
6 S. Kalluri, M. Yoon, M. Jo, H. K. Liu, S. X. Dou, J. Cho and Z. Guo, *Adv. Mater.*, 2017, **29**, 1605807.
7 S.-T. Myung, K. Izumi, S. Komaba, H. Yashiro, H. J. Bang, Y.-K. Sun and N. Kumagai, *J. Phys. Chem. C*, 2007, **111**, 4061–4067.
8 J. Chong, J. Zhang, H. Xie, X. Song, G. Liu, V. Battaglia, S. Xun and R. Wang, *RSC Adv.*, 2016, **6**, 19245–19251.
9 A. M. Wise, C. Ban, J. N. Weker, S. Misra, A. S. Cavanagh, Z. Wu, Z. Li, M. S. Whittingham, K. Xu, S. M. George and M. F. Toney, *Chem. Mater.*, 2015, **27**, 6146–6154.
10 A. Zhou, W. Wang, Q. Liu, Y. Wang, X. Yao, F. Qing, E. Li, T. Yang, L. Zhang and J. Li, *J. Power Sources*, 2017, **362**, 131–139.
11 Y. Zhang, Y. Tian, Y. Xiao, L. J. Miara, Y. Aihara, T. Tsujimura, T. Shi, M. C. Scott and G. Ceder, *Adv. Energy Mater.*, 2020, 1903778.
12 J. Zheng, M. Gu, J. Xiao, B. J. Polzin, P. Yan, X. Chen, C. Wang and J.-G. Zhang, *Chem. Mater.*, 2014, **26**, 6320–6327.
13 J.-Z. Kong, H.-F. Zhai, X. Qian, M. Wang, Q.-Z. Wang, A.-D. Li, H. Li and F. Zhou, *J. Alloys Compd.*, 2017, **694**, 848–856.
14 M. Bettge, Y. Li, B. Sankaran, N. D. Rago, T. Spila, R. T. Haasch, I. Petrov and D. P. Abraham, *J. Power Sources*, 2013, **233**, 346–357.
15 X. Zhang, I. Belharouak, L. Li, Y. Lei, J. W. Elam, A. Nie, X. Chen, R. S. Yassar and R. L. Axelbaum, *Adv. Energy Mater.*, 2013, **3**, 1299–1307.
16 Y. S. Jung, A. S. Cavanagh, A. C. Dillon, M. D. Groner, S. M. George and S.-H. Lee, *J. Electrochem. Soc.*, 2010, **157**, A75–A81.
17 J. S. Park, X. Meng, J. W. Elam, S. Hao, C. Wolverton, C. Kim and J. Cabana, *Chem. Mater.*, 2014, **26**, 3128–3134.
18 J. R. Croy, D. C. O'Hanlon, S. Sharifi-Asl, M. Murphy, A. Mane, C. W. Lee, S. E. Trask, R. Shahbazian-Yassar and M. Balasubramanian, *Chem. Mater.*, 2019, **31**, 3891–3899.
19 M. Aykol, S. Kim, V. I. Hegde, D. Snydacker, Z. Lu, S. Hao, S. Kirklin, D. Morgan and C. Wolverton, *Nat. Commun.*, 2016, **7**, 13779.
20 B. Liu, D. Wang, M. Avdeev, S. Shi, J. Yang and W. Zhang, *ACS Sustainable Chem. Eng.*, 2020, **8**, 948–957.
21 Y. Xiao, L. J. Miara, Y. Wang and G. Ceder, *Joule*, 2019, **3**, 1252–1275.
22 Z. A. Grady, C. J. Wilkinson, C. A. Randall and J. C. Mauro, *Front. Energy Res.*, 2020, **8**, 218.
23 V. Lacivita, N. Artrith and G. Ceder, *Chem. Mater.*, 2018, **30**, 7077–7090.
24 S. Xu, R. M. Jacobs, H. M. Nguyen, S. Hao, M. Mahanthappa, C. Wolverton and D. Morgan, *J. Mater. Chem. A*, 2015, **3**, 17248–17272.
25 G. Kresse and J. Furthmüller, *Comput. Mater. Sci.*, 1996, **6**, 15–50.
26 G. Kresse and J. Furthmüller, *Phys. Rev. B: Condens. Matter Mater. Phys.*, 1996, **54**, 11169–11186.
27 G. Kresse and D. Joubert, *Phys. Rev. B: Condens. Matter Mater. Phys.*, 1999, **59**, 1758–1775.
28 J. P. Perdew, K. Burke and M. Ernzerhof, *Phys. Rev. Lett.*, 1996, **77**, 3865–3868.
29 L. Martínez, R. Andrade, E. G. Birgin and J. M. Martínez, *J. Comput. Chem.*, 2009, **30**, 2157–2164.
30 J. Cheng, E. Sivonxay and K. A. Persson, *ACS Appl. Mater. Interfaces*, 2020, **12**, 35748–35756.
31 I. Enculescu and B. Iliescu, *Cryst. Res. Technol.*, 1997, **32**, 879–891.
32 J. Verhoogen, *Am. Mineral.*, 1952, **37**, 637–655.
33 M. R. Laskar, D. H. K. Jackson, S. Xu, R. J. Hamers, D. Morgan and T. F. Kuech, *ACS Appl. Mater. Interfaces*, 2017, **9**, 11231–11239.
34 K. D. Fong, J. Self, B. D. McCloskey and K. A. Persson, *Macromolecules*, 2020, **53**, 9503–9512.
35 R. Jung, M. Metzger, F. Maglia, C. Stinner and H. A. Gasteiger, *J. Electrochem. Soc.*, 2017, **164**, A1361–A1377.
36 T. Hatsukade, A. Schiele, P. Hartmann, T. Brezesinski and J. Janek, *ACS Appl. Mater. Interfaces*, 2018, **10**, 38892–38899.
37 S. S. Zhang, *Energy Storage Materials*, 2020, **24**, 247–254.
38 A. Jain, S. P. Ong, G. Hautier, W. Chen, W. D. Richards, S. Dacek, S. Cholia, D. Gunter, D. Skinner, G. Ceder and K. A. Persson, *Commentary: The Materials Project: A Materials Genome Approach to Accelerating Materials Innovation*, 2013.
39 M. Aykol, S. S. Dwaraknath, W. Sun and K. A. Persson, *Sci. Adv.*, 2018, **4**, eaaq0148.
40 M. W. Chase, J. L. Curnutt, J. R. Downey, R. A. Mcdonald, A. N. Syverud and E. A. Valenzuela, *J. Phys. Chem. Ref. Data*, 1982, **11**, 695–940.
41 A. Wang, R. Kingsbury, M. McDermott, M. Horton, A. Jain, S. P. Ong, S. Dwaraknath and K. A. Persson, *Sci. Rep.*, 2021, **11**, 1–10.
42 A. J. Bard, R. Parsons and J. Jordan, *Standard Potentials in Aqueous Solution*, 2017.
43 W. D. Richards, L. J. Miara, Y. Wang, J. C. Kim and G. Ceder, *Chem. Mater.*, 2016, **28**, 266–273.
44 Z. Chen, Y. Qin, K. Amine and Y. K. Sun, *J. Mater. Chem.*, 2010, **20**, 7606–7612.
45 I. Belharouak, C. Johnson and K. Amine, *Electrochem. Commun.*, 2005, **7**, 983–988.
46 J. W. Kim, D. H. Kim, D. Y. Oh, H. Lee, J. H. Kim, J. H. Lee and Y. S. Jung, *J. Power Sources*, 2015, **274**, 1254–1262.
47 X. Li, J. Liu, X. Meng, Y. Tang, M. N. Banis, J. Yang, Y. Hu, R. Li, M. Cai and X. Sun, *J. Power Sources*, 2014, **247**, 57–69.
48 L. Wang, X. Sun, J. Ma, B. Chen, C. Li, J. Li, L. Chang, X. Yu, T. S. Chan, Z. Hu, M. Noked and G. Cui, *Adv. Energy Mater.*, 2021, **11**, 2100881.

49 J. Geder, H. E. Hoster, A. Jossen, J. Garche and D. Y. Yu, *J. Power Sources*, 2014, **257**, 286–292.
50 S. W. Cho, G. O. Kim and K. S. Ryu, *Solid State Ionics*, 2012, **206**, 84–90.
51 Q. Gan, N. Qin, Z. Wang, Z. Li, Y. Zhu, Y. Li, S. Gu, H. Yuan, W. Luo, L. Lu, Z. Xu and Z. Lu, *ACS Appl. Energy Mater.*, 2020, **3**, 7445–7455.
52 Y. Zhu, X. He and Y. Mo, *ACS Appl. Mater. Interfaces*, 2015, **7**, 23685–23693.
53 B. D. McCloskey, R. Scheffler, A. Speidel, G. Girishkumar and A. C. Luntz, *J. Phys. Chem. C*, 2012, **116**, 23897–23905.
54 J. C. Deng, Y. L. Xu, L. Li, T. Y. Feng and L. Li, *J. Mater. Chem. A*, 2016, **4**, 6561–6568.
55 L. David, K. Dahlberg, D. Mohanty, R. E. Ruther, A. Huq, M. Chi, S. J. An, C. Mao, D. M. King, L. Stevenson and D. L. Wood, *ACS Appl. Energy Mater.*, 2019, **2**, 1308–1313.
56 J. Cheng, L. Mu, C. Wang, Z. Yang, H. Xin, F. Lin and K. Persson, *J. Mater. Chem. A*, 2020, **8**, 23293–23303.